

UC Berkeley

UC Berkeley Previously Published Works

Title

Mechanism of Nucleation and Growth of A β 40 Fibrils from All-Atom and Coarse-Grained Simulations

Permalink

<https://escholarship.org/uc/item/5x20x3z4>

Journal

The Journal of Physical Chemistry B, 120(47)

ISSN

1520-6106

Authors

Sasmal, Sukanya
Schwierz, Nadine
Head-Gordon, Teresa

Publication Date

2016-12-01

DOI

10.1021/acs.jpcb.6b09655

Peer reviewed

Mechanism of Nucleation and Growth of A β 40-Fibrils from All-Atom and Coarse-Grained Simulations

Sukanya Sasmal¹, Nadine Schwierz^{2,4} and Teresa Head-Gordon^{1,2,3,4*}

¹*Department of Chemical and Biomolecular Engineering,* ²*Department of Chemistry,*

³*Department of Bioengineering,*

⁴*Kenneth S. Pitzer Center for Theoretical Chemistry*

University of California, Berkeley, CA 94720, United States

***Corresponding author:**

Stanley 274

510-666-2744 (V)

[*thg@berkeley.edu*](mailto:thg@berkeley.edu)

ABSTRACT

In this work we characterize the nucleation and elongation mechanisms of the “diseased” polymorph of the amyloid- β 40 fibril by using an off-lattice coarse-grained (CG) protein model. After determining the nucleation size and subsequent stable protofibrillar structure from the CG model, validated with all-atom simulations, we consider the “lock and dock” and “activated monomer” fibril elongation mechanisms for the protofibril by the statistical additions of a monomer drawn from four different ensembles of the free amyloid- β 40 peptide to grow the fibril. Our CG model shows that the dominant mechanism for fibril elongation is the “lock and dock” mechanism across all monomer ensembles, even when the monomer is in the activated form. Although our CG model finds no thermodynamic difference between the two fibril elongation mechanisms, the “activated” monomer is found to be kinetically faster by a factor of two for the “locking” step compared to all other structured or unstructured monomer ensembles.

INTRODUCTION

The ability of the short 39-42 residue intrinsically disordered peptide amyloid- β (A β) to self-assemble into larger aggregates has long been ascertained to be a hallmark of Alzheimer's disease ¹. The peptide in its monomeric form is non-toxic, but it is prone to form both small soluble (oligomers) and large insoluble aggregates (fibrils) that get deposited into the brain of Alzheimer's patients as extracellular plaques ². Although there is mostly consensus that the lower molecular weight oligomers are the neurotoxic species ³, other work has argued that cytotoxicity of the insoluble fibrils could arise depending on the type of polymorph that is formed ⁴. Furthermore, recent work has indicated that the distinction between the two disease hypotheses may not be absolute, since oligomerization and early fibril formation pathways may be coupled. Chimon et al ⁵ and Ahmed and co-workers ⁶ have demonstrated that the early fibrillization pathway are connected through oligomerization intermediates, and fibrils have also been shown to catalyze toxic oligomer formation via secondary nucleation mechanisms ⁷. Thus, it remains important to understand the early stages of the A β fibril nucleation and elongation pathway given its potential connection to the disease state.

Amyloid fibril elongation is a complex process which can occur either by addition of structured/unstructured monomers at the fibril tips⁸ or by association of two smaller protofibrils to form a larger one ⁹. Recent experiments on the amyloidogenic α -synuclein fibril ⁸ using single-molecule localization microscopy have shown that monomer addition is the primary mechanism of fibril elongation, and amyloid fibrils have been experimentally shown to exhibit both unidirectional ¹⁰ and bidirectional growth ¹¹. In addition, fibrils do not have a uniform growth rate ¹², which can be explained by the "stop-and-go" model ¹³. According to this model, the fibrils interchange between the active "go" and inactive "stop" model, with only the active form taking part in amyloid elongation; any incorrect monomer addition makes the fibril template temporarily inactive, and monomer addition can resume only after the incorrectly added monomer has dissociated or attached itself in the correct alignment. The different spatial arrangements of the protofilaments that give rise to variations in the fibril structures have also been attributed to non-uniform fibril growth rates, highlighting the importance of understanding fibril polymorphism and the structural fluctuations that might contribute to different growth rates and mechanisms ⁸.

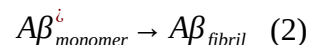
For a fibril in the "go" or active state, there are two proposed mechanisms for fibril elongation by monomer addition- the two-step "dock-lock" mechanism^{9, 14a, 14b, 14c} and the one-

step “activated” monomer mechanism^{14b, 14c}. The mechanistic model of the “dock-lock” mechanism is:



In the first step of the “dock-lock” mechanism, a structured/unstructured monomer binds reversibly, or “docks” to the fibril surface, and then in the “locking step”, the monomer undergoes structural rearrangements to form the native contacts present in a mature fibril. In previous studies the “locking” step is shown to be at least two orders of magnitude slower than the “docking” step¹⁵.

Unlike the “dock-lock” mechanism where the monomer goes through structural rearrangements after binding, in the “activated” monomer mechanism the free “monomer” in the solution is assumed to be present in the strand-loop-strand “U” shaped configuration adopted by peptide chains in mature fibrils. Schematically this process can be shown as:



where * represents the “activated” form. This “activated” monomer then irreversibly binds with the fibril surface and forms all the necessary native contacts in a one-step mechanism with a much faster time-scale.

There have been many computational studies looking at different aspects of A β fibril stability and growth processes using both atomistic and coarse-grained models to provide more molecular details that are outside of experimental purview. While all-atom simulations are able to look into specific residue and water interactions that may contribute to fibril stability and fibril growth mechanisms^{9, 14a, 16}, the timescale of fibril growth is on the order of milliseconds to several minutes¹⁷ which makes atomistic studies largely intractable for kinetic questions. Coarse-grained simulations¹⁸ and hybrid approaches¹⁹ have been shown to be promising in fibrillization studies, by providing for more statistically relevant data, after appropriate validation.

In this work, we have employed a coarse-grained (CG) protein model previously developed in our lab²⁰ in order to model the AD protofibril interacting with the A β monomer sampled from four different monomer ensembles: 1) monomers equilibrated under fibril potential, 2) a random coil monomer ensemble, 3) monomers obtained using a combination of all-atom simulations and experimental NMR data and 4) a so called “activated” monomer ensemble, which are described in more detail below. The CG model is able to capture the most important aspects of the complex physico-chemical properties of the amino acid beads and their sequence specific interactions, as well as the secondary structure propensities and tertiary

organization stabilized by van der Waals forces and short-ranged, anisotropic interactions that describe backbone hydrogen bonding. Early validation studies of our CG model demonstrated its ability to fold globular proteins with an RMSD of ~ 3 Å with respect to the native experimental structure^{20a-c, 21}, which is the limit possible under the coarse-graining procedure.

In the current study, we have extended the coarse-grained protein model to study the disease polymorph of amyloid fibril that has been recently solved by solid-state NMR²². Unlike the structural details of the oligomeric species which are mostly unknown, most amyloid fibrils are structurally defined by stacked in-register intermolecular β sheet filaments arranged with two-fold or three-fold symmetry about the fibril axis to create the insoluble fibril²³. *In vitro*, amyloid fibrils have been shown to be polymorphic, i.e. giving rise to structures that vary with different growth conditions²⁴. In fact we used the CG model to analyze the stability and growth mechanisms of the “agitated” and “quiescent” polymorphs of 2-stack A β 40 fibrils^{24a}, and familial Alzheimer’s disease (FAD) mutants^{18a, 18b, 25} in previous work. However recently Lu et al²² showed that fibrils grown from fibril seeds taken from the brain tissue of Alzheimer’s patients are not polymorphic, i.e. when exposed to different growth conditions, there is a single thermodynamically stable structural form, which we label the AD form. The solved AD fibril structure based on solid-state NMR consisted of a 3-fold symmetry arrangement of filaments, of which a few cross-sections involving only the backbone are shown in Figure 1.

In this work, we use the CG model to evaluate the nucleation and elongation free energy curve to determine the minimum number of monomers needed to stabilize the 3-stack AD A β 40 protofibril. Atomistic simulations have been used to validate the critical nucleus size obtained from the coarse-grained simulations, and are found to be in near quantitative agreement. Based on the minimal stable size of the AD protofibril, containing 15 peptide chains or 5 cross-sections, we have evaluated the fibril addition mechanism using four different monomer ensembles with the CG model. Our free energy of monomer addition is found to be in excellent agreement with experiment, and the 2-step “dock and lock” is the main mechanism for fibril elongation via monomer addition, irrespective of the monomer configuration ensemble. Kinetically, we find that the docking step is anywhere between 4X and 28X faster than the locking step depending on monomer ensemble, with the activated monomer exhibiting much faster growth on the C-terminus of the fibril compared to all other monomer conformational ensembles.

METHODS

Details of the Coarse-Grained Model. Each amino acid of the CG protein model is represented by a single bead corresponding to C_α carbon atom positions. The $C_\alpha - C_\alpha$ distance are scaled by the characteristic length scale σ_o , which is set to a fixed value of 3.808 Å, corresponding to the average distance between two adjacent C_α atoms when the intervening peptide bond is in the trans state. The energy function used in the CG model is

$$E_{total} = \sum_{\text{angles}} \frac{1}{2} k_\theta (\theta - \theta_0)^2 + \sum_{\text{dihedrals}} \left[\begin{array}{l} A [1 + \cos(\phi + \phi_0)] + B [1 - \cos(\phi + \phi_0)] \\ + C [1 + \cos 3(\phi + \phi_0)] + D \left[1 + \cos \left(\phi + \phi_0 + \frac{\pi}{4} \right) \right] \end{array} \right]$$

$$+ \sum_{\substack{i, j \geq 3 \text{ for intrachain} \\ i, j \text{ for interchain}}} 4 \epsilon_H S_1 \left[\left(\frac{\sigma}{r_{ij}} \right)^{12} - S_2 \left(\frac{\sigma}{r_{ij}} \right)^6 \right] + \sum_{\text{Hbonds}} U_{HB} \quad (3)$$

where the first term represents the angle-

bending potential, modeled as a stiff harmonic potential with a spring constant $k_\theta = 20 \epsilon_H / \text{rad}^2$ and θ is the bond angle defined by three consecutive C_α beads. The optimal bond angle θ_0 is set to 95° if bead i is involved in helical secondary structure, 120° if in beta sheets and 105° otherwise. The second term is the dihedral angle potential, where A, B, C, D and ϕ_0 are constants whose values are adjusted to get the desired minima and energy barrier for different dihedral types (Table S1 and Figure S1) formed by beads $i-1, i, i+1$ and $i+2$. There are six different types of dihedrals – helical (H), extended (E), floppy turn (T), $\pm 90^\circ$ turns (P/Q) and 0° dihedral turns (U).

The third term describes the potential involving non-local interactions (Figure S2), where r_{ij} is the distance between beads i and j , and σ is set to $1.16 \sigma_o$ to account for the excluded volume of the side chains. There are four different bead flavors – strong attraction (B), weak attraction (V), weak repulsion (N) and strong repulsion (L), and the values of S correspond to different bead–bead interactions. $S_2 = -1$ for the attractive interaction B-B, B-V and V-V, while $S_1 = 1.4, 0.7$ and 0.35 respectively. $S_1 = 1/3$ and $S_2 = -1$ for repulsive interactions L-L, L-V and L-B; and $S_1 = 0.35$ and $S_2 = 0$ for all repulsive N-X interactions.

The last term U_{HB} is a distance and orientation dependent short-ranged function for hydrogen bonding interactions. The energy U_{HB} between beads i and j is given by:

$$U_{HB} = -\epsilon_{HB} F(r_{ij} - r_{HB}) G(|t_{HB,i} \cdot \hat{r}_{ij}| - 1) G(|t_{HB,j} \cdot \hat{r}_{ij}| - 1) \quad (4a)$$

$$F(r_{ij} - r_{HB}) = \exp \left[\frac{-(r_{ij} - r_{HB})^2}{\sigma_{HBdist}^2} \right] \quad (4b)$$

$$G(|t_{HB,i} \cdot \hat{r}_{ij}| - 1) = \exp\left[\frac{|t_{HB,i} \cdot \hat{r}_{ij}| - 1}{\sigma_{HB}^2}\right] (4c)$$

where F is a Gaussian distance dependent term centered at the ideal hydrogen bond distance r_{HB} , and $r_{HB} = 1.35 \sigma_o$ for helices and $1.25 \sigma_o$ for all other secondary structure types. The directional dependent terms, G , have an exponential form, whose arguments $t_{HB,i}$ and $t_{HB,j}$ are unit normal vectors to the planes described by beads $i-1, i, i+1$ and beads $j-1, j, j+1$ respectively. The width of the functions F and G are both set to $\sigma_{HBdist} = \sigma_{HB} = 0.5$. The energy scale is set by the hydrophobic strength ϵ_H .

The hydrogen bonding capabilities of a given amino acid are classified as follows: helical (A), extended β -strand that can form both intramolecular and intermolecular hydrogen-bonds (B), both helical/extended (X), extended β -strand that can form only intermolecular hydrogen-bonds (Y), and none (C). In this work we have extended the intramolecular hydrogen-bond interactions to now describe intermolecular hydrogen-bonding through the new classification Y. For beads assigned as helix, the U_{HB} term is evaluated between i and $i+3$ bead pairs, and for beads assigned as beta sheets (B/Y) or both (X), the term is evaluated for every bead pair within a cutoff distance of $3.0 \sigma_o$.

AD Fibril Model and the different A β 40 Monomer Ensembles. The starting structure of the CG A β 40 AD fibril was modeled on the 3-stack fibril structure determined by Lu et al. (PDB ID 2M4J) (12). Each amino acid of A β 40 is represented by a single bead corresponding to its C_α carbon atom positions, and Table 1 provides the sequence mapping for the A β 40 peptide, and additional information about the secondary structure propensities and hydrogen bonding capabilities of each residue. Details about mapping the amino acids to CG beads are provided in the SI.

In order to study fibril elongation by monomer addition at the fibril ends, we have adopted 4 different coarse-grained monomer ensembles. Details about the force field used for the monomer ensemble can be found in Table 2, but they are summarized here.

(1) For the first monomer ensemble, referred to as the *Fibril* ensemble, we have used individual monomers derived from the middle cross-sections of protofibrils equilibrated with the coarse-grain potentials. The monomer potential is then exactly the same as the fibril potential (Table 1). However, in the absence of other ‘‘U-shaped’’ adjacent monomers with which to form intermolecular interactions, the monomers can instead form intra-molecular β -strand when they are equilibrated alone in the box.

(2) The second ensemble, the *Random* ensemble, has monomers whose secondary structure for all the beads are designated as a “floppy turn T”, but with the ability to form intramolecular or intermolecular hydrogen bonds with any other bead.

(3) The third ensemble, the *IDP* ensemble, is a CG ensemble based on the all-atom simulations by Ball and co-workers, which was shown to form a diverse set of partial secondary structures²⁶. The all-atom *IDP* ensemble was generated from a Replica Exchange molecular dynamics simulations²⁶, and then using the ENSEMBLE conformer selection program²⁷ to select the best set of structures that conform to experimental NMR data, including chemical shifts and J-couplings²⁸. While the bead flavor for each residue is (by definition) the same as the fibril monomers, another new advance of the CG model methodology is that each individual monomer now has distinct tertiary conformations, and thus different bead secondary structure propensities and hydrogen bonding abilities. In this study the individual monomer potentials are determined using the DSSP criterion²⁹.

(4) Finally, the *Activated* monomer ensemble was restrained to conform to the same shape found in mature AD fibrils, such that they are always in the “activated” form. The barriers for the intramolecular β -strand potential have been increased (γ dihedral), so that the monomers have higher probability of being in the strand-loop-strand fibrillar form, and they are less likely to form intramolecular hydrogen bonds.

Simulation protocol for the CG model. Constant temperature Langevin dynamics was used to propagate the simulation. The simulations are done in reduced units with mass m , energy ϵ_{HB} , length σ_o and k_B being set to unity. The bond length between adjacent beads are held constant using RATTLE algorithm³⁰. Reduced time and temperature are given by $\tau = (m\sigma_o/\epsilon_H)^{1/2}$ and $T^* = \epsilon_H/k_B$. We simulated the systems at reduced temperature $T^*=0.45$ (~ 337 K) with a timestep of 0.005τ and friction parameter $\zeta=0.05$. Based on a reasonable energy criteria for hydrogen-bonding, our estimated time step using the CG model is ~ 1 ns. The simulation box size is 150 reduced units in all dimensions.

Fibril Stability Metric. For the fibril stability studies, a long AD amyloid fibril consisting of 24 cross-sections (72 monomer chains total) was first equilibrated for 1.3M time steps in the *NVT* ensemble at the reduced temperature $T^* = 0.45$ ($T \approx 337$ K). Models for different fibril sizes from 6 monomer chains (2 cross-sections) to 30 monomer chains (10 cross-sections) were made from the inner-most center of the equilibrated long AD fibril. We performed 24 independent equilibration runs for the longer fibrils, followed by 3 simulations for each of the smaller

protofibrils obtained from the larger fibrils in the NVT ensemble at the same T^* . We thus collected production statistics of 120 independent runs for each fibril size, with the simulation time for each run being 65000τ or 13M time steps, corresponding to roughly 13 ms for each simulation.

Protofibril structural stability is measured from the order parameter, χ .

$$\chi = \frac{1}{M} \sum_{\alpha=1}^{N_c} \sum_{\beta>\alpha}^{N_c} \sum_i^N \sum_j^N h\left(\varepsilon - \left| r_{\alpha,i;\beta,j} - r_{\alpha,i;\beta,j}^0 \right| \right) \quad (5)$$

where the outer two sums are over all chains α and β of the outermost two cross-sections of the two ends of the protofibrils, and the inner sums are over bead i of chain α and bead j of chain β , and M is the total number of pair distances. The scalar $r_{\alpha,i;\beta,j}$ corresponds to the distance between bead i on chain α and bead j on chain β of a given protofibrils configuration, while $r_{\alpha,i;\beta,j}^0$ defines the same distance but for the reference AD protofibril. The χ value gives an estimate of the structural deviations from the ideal AD protofibril structure, and since it is based on the Heaviside function, h , it ranges from 0 to 1, with a value of 1 indicating perfect structural agreement with the ideal AD reference within allowed thermal fluctuations, ε (set to 0.6 distance units or 2.3 Å). Since the order parameter only takes into account the outermost two cross-sections, it can be used for direct comparison between AD protofibrils containing any larger number of cross-sections.

We use two forms of the χ parameter defined in Eq. (5), by restricted sums over beads and chains in Eq. (5). The first metric P_f measures the local structural similarity of the individual protofilaments to the AD reference protofilament, by looking at chain pairs α and β belonging to only one protofilament. It thus sums over 3 independent chain pairs at each end, and only considers beads i and j for residues 17-35 residues which includes the two β strands and the connecting turn region. The global χ_f metric measures how the 3 protofilaments are oriented with respect to one another and with the fibril axis. In this case the chains α and β correspond to the six monomer chains on each end, and the sum over beads i and j are restricted to the β strand regions 17-21 and 31-35. In both cases, statistics were collected about after every 50τ (10,000 steps).

Free Energy Protocol for the CG model. Based on the fibril ensembles generated for the AD protofibrils of different numbers of cross-sections, we can calculate equilibrium populations of structurally stable and unstable protofibrils based on population differences measured by either P_f and/or χ_f . We have determined that there are two well-defined and reasonably well-

separated populations, one of which is defined by $P_f > 0.7$ and $\chi_f > 0.7$ which measures a population, C_n , of n -ordered monomers in a protofibril with intact end monomers and a well-defined fibril axis. This population is in equilibrium with the remaining fraction of trajectories corresponding to a protofibril with loss of structural order corresponding to $P_f < 0.7$ or $\chi_f < 0.7$, and thus measures the population C_{n-1} .

Based on thermodynamic arguments advanced by Ferrone³¹ for nucleation-polymerization reactions, we can estimate the change in free energy, ΔG , per unit cross-section, n , as

$$\frac{d\Delta G}{dn} = k_B T \ln \left(\frac{[C_{n-1}]}{[C_n]} \right) \quad (6)$$

where k_B is the Boltzmann constant and T is the temperature. When

Eq. (6) is integrated over all oligomer sizes, we can generate a free energy curve based on C_n and C_{n-1} populations measured in our model, to determine the critical nucleus size and size regime in which the fibril is thermodynamically stable.

All-atom simulation protocol. The fibrils for the structural stability analysis in the all-atom MD simulations consisted of 3-15 A β 40 peptide chains, based on the 2M4J AD amyloid fibril²². All amino acid termini are capped using an uncharged amino group at the N-terminus and an uncharged carboxyl group at the C-terminus. In our model, residues K16 and K28 are positively charged and residues E11, E22 and D23 are negatively charged based on neutral pH, physiological salt concentration and the pKa values of the amino acids. This results in one excess negative charge for each peptide., and the system is neutralized with 0.15 M NaCl, leading to a system size of up to 224,000 atoms. The force field parameters for the peptides are taken from Amber99sb-star-ildn³², TIP4P-Ew is used for the water molecules³³. The simulation box has the size of 120 Å in all directions.

The molecular dynamics simulations at fixed particle number N , pressure P and temperature T are performed using the Gromacs simulation package, version 4.6.1³⁴. Periodic boundary conditions are applied and the particle-mesh Ewald method is used for the periodic treatment of Coulomb interactions. The bonds to hydrogen atoms are constrained by the LINCS algorithm³⁵ and a 2 fs time step is used. To equilibrate the system, we first perform an energy minimization with the steepest descent algorithm. We employ 200 ps first in the NVT and then in the NPT ensembles as equilibration using the Berendsen scheme. For the production run, we perform 100 ns simulations employing Nosé-Hoover temperature coupling with a time constant

of $\tau_T = 0.5\text{s}^{-1}$ and isotropic Parrinello-Rahman pressure coupling with a time constant of $\tau_p = 5\text{s}^{-1}$. Conformational transitions are quantified using the same two order parameters used for the CG model.

Molecular Graphics: The molecular graphics were created using the Visual Molecular Dynamics (VMD) software package³⁶ <http://www.ks.uiuc.edu/Research/vmd/>

RESULTS

Fibril stability and critical nucleus of the AD fibril. We examined AD protofibrils of different numbers of cross-sections ranging from 2 to 10 (i.e. 6-30 monomer chains) to determine the critical nucleus and the size regime where the AD fibril becomes stable. In each case the fibril order was tracked as a function of time using the fibril structural similarity parameters χ_f and P_f as described in the Methods section. Figure 2 shows the average of the two metrics, $\langle\chi_f\rangle$ and $\langle P_f\rangle$ taken over the last 5000 τ of simulation for the two fibril ends. Both $\langle\chi_f\rangle$ and $\langle P_f\rangle$ show an increasing trend of stability with increasing number of cross-sections in the protofibrils, which flattens out beyond 5 cross-sections. As expected, $\langle P_f\rangle$ has a higher value than the $\langle\chi_f\rangle$ metric, indicating that there is less disorder at the individual protofilament level as compared to the quaternary arrangement of the protofilaments in the protofibril.

A characteristic of the amyloid fibril is interdigitation^{24a} of the N-terminal and C-terminal β -strands of two distinct chains to form side-chain hydrophobic contacts, known as the “stagger” in amyloid fibril terminology. For the agitated polymorph of the 2-stack fibril, the side-chains of the N-termini of chain i interacts with the C termini of monomer $i+2$ to yield a stagger value of +2. We have shown in previous work that the fibril stagger results in asymmetry in the fibril ends^{18a}, such that one end has the C-termini exposed while and the other end exposes the N-terminus. For the AD fibrils, the side-chains of the N-termini of chain i interacts with the C termini of monomer $i+1$, i.e. a stagger value of +1.

Our analysis shows that the smaller protofibrils have similar fibril similarity parameter values at each of the ends, until 4 cross-sections are formed, after which the $\langle\chi_f\rangle$ and $\langle P_f\rangle$ values start showing differences between the two protofibril ends when the fibril stagger becomes more prominent. Furthermore, the most common signature of instability at the fibril ends in our simulations is when the end monomers form intra-molecular β -hairpins instead of inter-molecular β -strands (Figure 3). Both explicit⁹ and implicit water simulations^{16a} have confirmed that one of the possible intermediates during fibril elongation is the formation of such

β -hairpins. Our CG simulations thus suggest similar intermediates for fibril dissociation at the tips.

Figure 4 plots the free energy as a function of the number of cross-sections in the protofibrils based on integration of Eq. (6). The nature of the free energy profile corresponds to what one would expect for nucleated growth polymerization, with the critical nucleus being the most unstable species. In our CG model the critical nucleus size is ~ 12 peptide chains or 4 cross-sections, in which the protofibril has well-formed intermolecular β sheets, but either exhibits point chain defects (like the β -hairpin) or lacks the specific quaternary interactions present in the mature fibrils such as a well-defined stagger. Below the critical nucleus size, the equilibrium shifts towards free monomers while beyond the critical nucleus size the protofibril is dominated by a population that is able to maintain the AD fibril structure, and subsequent addition of cross-sections increases the thermodynamics stability of the fibril species. It should be noted that we are not on an absolute scale for free energy, and therefore impose the definition of zero at the minimum protofibril size.

In order to validate the free energy results obtained from our coarse-grain model, we performed 100 ns simulations of 2 to 5 cross-sections (6-15 peptide chains) to see whether we obtain similar structural stability trends using all-atom simulations with explicit water. We used the same global χ_f and local P_f metrics (Eq. (5)) calculated for the N-terminus and C-terminus, with ϵ set to 2.3 Å, which is equivalent to the CG value after adjustments from reduced units. Figure 5 shows $\langle \chi_f \rangle$ and $\langle P_f \rangle$ metrics averaged over the last 30 ns, and Figures S3 and S4 show the full 100ns time course using these same metrics. Like the CG model, individual protofilaments are better ordered with respect to the overall protofibril metric, and in general the C-terminus has higher values than the N-terminus. The global χ metric shows an increasing trend to stability, and reaches an abrupt convergence at 15 peptide chains. The large variation in the order parameter at 12 chains is consistent with the CG model, the size at which the protofibril corresponds to the most unfavorable free energy in the thermodynamics of fibril stability. Thus the all-atom model strongly supports the size at which we can investigate the thermodynamics and kinetic mechanisms of fibril addition in what follows.

Thermodynamics of Fibril Elongation. In order to evaluate the thermodynamics of fibril elongation for the CG model, and its dependence on the monomer ensemble, we picked the stable form of the model protofibril containing 5 cross-sections and added it to the simulation box populated randomly with 10 monomers drawn from each of the four monomer ensembles.

The peptides were allowed to diffuse for 65M time steps (estimated to be 65 milliseconds) at $T^*=0.45$ during which we collected statistics on the probability function $p(r_c)$, the probability of finding the center of mass of a “free” monomer at a distance r_c from the mid-point of the outermost fibril cross-section. The mid-point of fibril cross-section is defined as the centroid of the triangle formed by bead 33 of the three peptides chains forming the cross-section. The probability $p(r_c)$ was normalized by the probability of finding a monomer in the bulk. We considered only the monomers that add on to the fibril tips, and ignore monomers that take part in lateral addition to the fibril surface, by constructing a half-spherical shell with the mid-point of the outermost fibril cross-section as the origin in $p(r_c)$ calculation. This definition is consistent with the experiment in reference 57, which monitored the increase in Thioflavin T fluorescence resulting from binding of the fluorescent dye to β -sheets present in amyloid structure; thus, the experimental technique reports only on monomer binding at the fibril tips, and not on the lateral edges. The other half-sphere, which we have ignored in our calculations, contains the middle cross-sections of the fibril where monomers are more likely to take part in lateral addition; our calculations showed that only 1-2% of the monomers ended up in the ignored half-spherical region, and thus the numbers we have presented in this paper for binding affinities won't be significantly influenced by the choice of our shell.

One dimensional free energy profile (so called potential of mean force, PMF) sampled along the radial distance r from the fibril tip, is then calculated as

$$F(r_c) = -k_B T \ln[p(r_c)] \quad (7)$$

Standard deviations are based on five different sets of runs, with each set of run consisting of 300 separate simulations. Figure 6 shows the reversible work needed for a monomer to move from the fibril surface to a separation distance r_c between the fibril end and the monomers sampled from the *Fibril* ensemble (Fig. 6a) and from the *Activated* ensemble (Fig. 6b); we include the same PMF plots for the *Random* and *IDP* monomer ensembles in the SI material. In all four cases the PMF plot has a single minima and shows no difference at the two fibril ends. The one-dimensional PMF, based solely on the distance of separation between the monomer and the fibril surface, largely captures the free energy of the “docking” phase.

We next proceed to estimating the free energy of binding (ΔG_{Bind}) derived by Schwierz et al.⁹ using Eq. (8) .

$$k_{EQ} = L_x L_y \int_{r_B}^{r_S} dr_C \frac{P(r_C)}{P(r_S)} \quad (8a)$$

$$\Delta G_{Bind} = k_B T \ln [c^0 k_{EQ}] \quad (8b)$$

where k_{EQ} is the equilibrium constant for peptide binding, L_x and L_y are the dimensions of the simulation box, r_S is the smallest separation distance where $F(r_C) \approx 0$, r_B is the separation distance corresponding to minimum value of $F(r_C)$, $P(r_C)$ is the simulated probability density distribution, and c^0 is standard state concentration (1 mol/L). Table 3 provides the calculated free energy of binding for the different monomer ensembles using the CG model, which varies from 13.3-14.3 $k_B T$. These values are in very good agreement with experimental binding affinities of $\sim 15.2 k_B T$ ³⁷, and suggests that the lack of explicit interactions due to water and side chain degrees of freedom are not strongly effecting the results, in which all atom simulations determined binding free energies of $\sim 8-10 k_B T$ ⁹.

Since all four ensembles have similar PMF values and free energy of binding within thermal fluctuations, the “docking” phase is found to not be sensitive to the monomer conformational ensemble. The optimal r_C for the C-terminus is slightly lower than the N-terminus by $\sim 2.3 \text{ \AA}$ for all the ensembles except the *Activated* ensemble. Since the C-terminal tip has more hydrophobic residues, which manifests as a higher density of attraction in our model, the approaching monomer has more non-specific surface area to explore when “docking” and is more collapsed when it docks. On the other fibril end, the N-terminus has more sequence specificity and patterning of both attractive and repulsive beads, hence the monomer requirements for finding optimal interactions is more entropically unfavorable. Because the monomers of the *Activated* ensemble are very rigid with a fixed shape, these monomers don’t collapse upon docking on the C-terminus, and thus have similar separation distance r_C at the two fibril ends.

Kinetics of Fibril Elongation. We next performed simulations to evaluate the mean first passage time (MFPT) for fibril elongation by monomer addition. The simulation conditions comprised an equilibrated stable protofibril with 15 peptide chains as before, but now with two monomers placed randomly on either side of the fibril such that the separation between bead 20 of the monomer and the mid-point of the outermost fibril cross-section was 5 reduced distance units ($\sim 19 \text{ \AA}$). This initial condition minimized any lag time resulting from the time to encounter the fibril tip by diffusion, and the large simulation box size ensured that the two monomers at the two opposite ends of the protofibril did not interact with each other. The upper bound for the

MFPT was 65M time steps (~65 ms) at $T^*=0.45$, and again the 1500 independent trajectories were divided into five sets to calculate standard deviations.

It is difficult to observe a complete “dock-lock” or “activated” monomer addition mechanism using even CG computer simulations owing to the slow time scale in the range of minutes¹⁵. To overcome this problem and at the same time get some meaningful information about the mechanisms, we looked at the MFPT required to form the first 5 non-native contacts as an estimate of the docking time, and 5 native contacts as a lower bound to the locking time scale. Since the “docking” step is a reversible process, with monomers forming and breaking contacts, we found that the rate of monomer dissociation from the fibril tip was more than 50% when fewer than 5 contacts were formed between the free monomer and fibril tip, hence why we selected a lower bound of 5 non-native contacts. We choose the same number for the native contacts in the “locking” step to be consistent with our definition of “docking” step, where in this case the first 5 native contacts are restricted to residues 8-40, which take part in inter-molecular β -sheets and also in hydrophobic contacts between different protofilament layers.

Figure 7a shows the MFPT needed to form the first five non-native in the docking step and the first five native contacts in the locking step between the free monomer and for the two fibril ends. The time-scale for forming the non-native contacts at the two fibril tips are very similar for all monomer ensembles except the Activated monomer ensemble which shows addition to the C-terminus that is 3 to 4 times faster than addition to the N-terminus. Figure 7b shows the MFPT needed to form the first 10 non-native in the docking step and the first 10 native contacts in the locking step between the free monomer and for the two fibril ends, confirming that the results are not changed by the choice of the number of native/non-native contacts. Figure S6 and S7 shows representative snapshots of fibril structures during elongation process, with monomers forming 5 native and non-native contacts.

Furthermore there are distinctly different time-scales associated with the “docking” phase, which is any where from 4X to 30X times faster than the start of the “locking” phase depending on monomer ensemble, with the smallest difference observed for *Activated* monomer addition to the C-terminus of the fibril (Table 4). These timescales are distinct enough such that we can state that even the *Activated* monomer first “docks” onto the fibril surface at non-specific locations and has to search on the fibril surface to form the “correct” specific contacts. For the “activated monomer” mechanism, one would expect more commensurate time-scales for the formation of first five non-native and native contacts – something that we do not strictly observe

in our simulations. Even so, the start of the locking step is two times faster for the *Activated* monomer ensemble compared to other monomer ensembles since it doesn't require any internal reconfiguration to properly "lock", especially on the C-terminus end of the fibril.

DISCUSSION AND CONCLUSIONS

A detailed understanding of the mechanism underlying nucleation and growth of amyloid fibrils is a fundamental question that relates to possible disease origins for neurodegenerative conditions such as Alzheimer's disease. However, due to the slow millisecond to second experimental time scale involved in amyloid fibril formation, all-atom computer simulations that can provide molecular interpretations are challenged by the restrictions of the computational time scale of microseconds at most. In this case coarse-grained simulations have proven very useful by integrating out uninteresting fast motions to reach effective timescales of tens of milliseconds in order to obtain mechanistic information on the nucleation and first events of fibril elongation of the diseased polymorph of amyloid fibrils composed of the A β 40 peptide.

Both the CG and all-atom simulations corroborate that the critical nucleus is ~ 12 A β peptide chains, and that the minimal size at which AD protofibrils become stable correspond to 15 A β peptide chains arranged in 5 cross-sections. For the fibril elongation process, we tested the 2-step dock-lock mechanism, in which the docked peptide undergoes significant conformational rearrangements to fit precisely on the fibril template, and the activated monomer mechanism in which the peptide is already in the U-shaped conformation observed in a mature fibril and is hypothesized to add onto the fibril in a single step. Our results show that there is no significant thermodynamic difference between the two scenarios, and that the kinetics in both cases is always a 2-step process involving a docking timescale that is 4X to 30X faster than the locking step, depending on which fibril end on which addition takes place, and the type of monomer ensemble.

To form at least 5 native contacts between the fibril and the monomer in the locking step indicates that the conformational rearrangements of a non-activated peptide is ~ 2 X slower than the rotational rearrangement of the activated but ridged U-shaped peptide. While the activated monomer conformation is rare, making up to 1-5% of the conformational ensemble derived from all-atom simulations that best conform to the NMR data for A β monomers in solution²⁸, the CG

models suggest that the kinetics of fibrillization would be faster with an activated form of the monomer, with more biased unidirectional growth on the C-terminus.

SUPPORTING INFORMATION.

Details about assignment of bead flavors to the A β peptide sequence are presented in the Methods section and Table S1. More information about force-field parameters can be found in Figure S1 (dihedral angle potential) and S2 (non-bonded interaction potential). Figure S3 and S4 show the time-course of the fibril similarity parameters P_f and χ_f respectively for the all-atom simulations. The plots for the potential of mean force ($F(\delta_c)$) profile for monomer addition at the two fibril tips for the *Random* and *IDP* ensemble is given in figure S5. Lastly, figure S6 and S7 are representative snapshots showing the “docking” and “locking” step for the “lock and dock” mechanism of fibril elongation.

ACKNOWLEDGEMENTS. THG thanks the National Science Foundation grant CHE-1363320 for support of this work. NS thanks the Alexander von Humboldt Foundation for financial support. This research used resources of the National Energy Research Scientific Computing Center, a DOE Office of Science User Facility supported by the Office of Science of the U.S. Department of Energy under Contract No. DE-AC02-05CH11231.

REFERENCES

1. Karran, E.; Mercken, M.; De Strooper, B., The amyloid cascade hypothesis for Alzheimer's disease: an appraisal for the development of therapeutics. *Nature Rev. Drug Disc.* **2011**, *10* (9), 698-712.
2. Glabe, C. G., Structural classification of toxic amyloid oligomers. *J. Biol. Chem.* **2008**, *283* (44), 29639-29643.
3. (a) Walsh, D. M.; Klyubin, I.; Fadeeva, J. V.; Cullen, W. K.; Anwyl, R.; Wolfe, M. S.; Rowan, M. J.; Selkoe, D. J., Naturally secreted oligomers of amyloid β protein potently inhibit hippocampal long-term potentiation in vivo. *Nature* **2002**, *416* (6880), 535-539; (b) Haass, C.; Selkoe, D. J., Soluble protein oligomers in neurodegeneration: lessons from the Alzheimer's amyloid β -peptide. *Nature Rev. Mol. Cell Biol.* **2007**, *8* (2), 101-112.
4. Petkova, a. T.; Leapman, R. D.; Guo, Z. H.; Yau, W. M.; Mattson, M. P.; Tycko, R., Self-propagating, molecular-level polymorphism in Alzheimer's beta-amyloid fibrils. *Science* **2005**, *307* (5707), 262-265.
5. Chimon, S.; Shaibat, M. A.; Jones, C. R.; Calero, D. C.; Aizezi, B.; Ishii, Y., Evidence of fibril-like β -sheet structures in a neurotoxic amyloid intermediate of Alzheimer's β -amyloid. *Nature Struct .Biol.* **2007**, *14* (12), 1157-1164.
6. Ahmed, M.; Davis, J.; Aucoin, D.; Sato, T.; Ahuja, S.; Aimoto, S.; Elliott, J. I.; Van Nostrand, W. E.; Smith, S. O., Structural conversion of neurotoxic amyloid-[beta] 1-42 oligomers to fibrils. *Nature Struct .Biol.* **2010**, *17* (5), 561-567.

7. Cohen, S. I.; Linse, S.; Luheshi, L. M.; Hellstrand, E.; White, D. A.; Rajah, L.; Otzen, D. E.; Vendruscolo, M.; Dobson, C. M.; Knowles, T. P., Proliferation of amyloid- β 42 aggregates occurs through a secondary nucleation mechanism. *Proc. Natl. Acad. Sci.* **2013**, *110* (24), 9758-9763.
8. Pinotsi, D.; Buell, A. K.; Galvagnion, C.; Dobson, C. M.; Kaminski Schierle, G. S.; Kaminski, C. F., Direct observation of heterogeneous amyloid fibril growth kinetics via two-color super-resolution microscopy. *Nano Lett.* **2013**, *14* (1), 339-345.
9. Schwierz, N.; Frost, C. V.; Geissler, P. L.; Zacharias, M., Dynamics of Seeded A β 40-Fibril Growth from Atomistic Molecular Dynamics Simulations: Kinetic Trapping and Reduced Water Mobility in the Locking Step. *J. Am. Chem. Soc.* **2016**, *138* (2), 527-539.
10. Ban, T.; Hoshino, M.; Takahashi, S.; Hamada, D.; Hasegawa, K.; Naiki, H.; Goto, Y., Direct observation of A β amyloid fibril growth and inhibition. *J. Mol. Biol.* **2004**, *344* (3), 757-767.
11. (a) Pinotsi, D.; Buell, A. K.; Galvagnion, C.; Dobson, C. M.; Kaminski Schierle, G. S.; Kaminski, C. F., Direct observation of heterogeneous amyloid fibril growth kinetics via two-color super-resolution microscopy. *Nanoletters* **2013**, *14* (1), 339-345; (b) Blackley, H.; Sanders, G.; Davies, M.; Roberts, C.; Tendler, S.; Wilkinson, M., In-situ atomic force microscopy study of β -amyloid fibrillation. *J. Mol. Biol.* **2000**, *298* (5), 833-840.
12. Kellermayer, M. S.; Karsai, Á.; Benke, M.; Soós, K.; Penke, B., Stepwise dynamics of epitaxially growing single amyloid fibrils. *Proc. Natl. Acad. Sci.* **2008**, *105* (1), 141-144.
13. Ferkinghoff-Borg, J.; Fonslet, J.; Andersen, C. B.; Krishna, S.; Pigolotti, S.; Yagi, H.; Goto, Y.; Otzen, D.; Jensen, M. H., Stop-and-go kinetics in amyloid fibrillation. *Phys. Rev. E* **2010**, *82* (1), 010901.
14. (a) Nguyen, P. H.; Li, M. S.; Stock, G.; Straub, J. E.; Thirumalai, D., Monomer adds to preformed structured oligomers of A β -peptides by a two-stage dock-lock mechanism. *Proc. Natl. Acad. Sci.* **2007**, *104* (1), 111-116; (b) Straub, J. E.; Thirumalai, D., Toward a molecular theory of early and late events in monomer to amyloid fibril formation. *Ann. Rev. Phys. Chem.* **2011**, *62*, 437-463; (c) Massi, F.; Straub, J. E., Energy landscape theory for Alzheimer's amyloid β -peptide fibril elongation. *Proteins: Struct., Func., Bioinform.* **2001**, *42* (2), 217-229.
15. Esler, W. P.; Stimson, E. R.; Jennings, J. M.; Vinters, H. V.; Ghilardi, J. R.; Lee, J. P.; Mantyh, P. W.; Maggio, J. E., Alzheimer's disease amyloid propagation by a template-dependent dock-lock mechanism. *Biochem.* **2000**, *39* (21), 6288-6295.
16. (a) Gurry, T.; Stultz, C. M., Mechanism of amyloid- β fibril elongation. *Biochemistry* **2014**, *53* (44), 6981-6991; (b) Buchete, N.-V.; Tycko, R.; Hummer, G., Molecular dynamics simulations of Alzheimer's β -amyloid protofilaments. *J. Mol. Biol.* **2005**, *353* (4), 804-821; (c) Buchete, N.-V.; Hummer, G., Structure and dynamics of parallel β -sheets, hydrophobic core, and loops in Alzheimer's A β fibrils. *Biophys. J.* **2007**, *92* (9), 3032-3039; (d) Horn, A. H.; Sticht, H., Amyloid- β 42 oligomer structures from fibrils: a systematic molecular dynamics study. *J. Phys. Chem. B* **2010**, *114* (6), 2219-2226.
17. (a) Cannon, M. J.; Williams, A. D.; Wetzell, R.; Myszka, D. G., Kinetic analysis of beta-amyloid fibril elongation. *Anal. Biochem.* **2004**, *328* (1), 67-75; (b) Qiang, W.; Kelley, K.; Tycko, R., Polymorph-specific kinetics and thermodynamics of β -amyloid fibril growth. *J. Am. Chem. Soc.* **2013**, *135* (18), 6860-6871.
18. (a) Fawzi, N. L.; Okabe, Y.; Yap, E.-H.; Head-Gordon, T., Determining the critical nucleus and mechanism of fibril elongation of the Alzheimer's A β 1-40 peptide. *J. Mol. Biol.* **2007**, *365* (2), 535-550; (b) Fawzi, N. L.; Kohlstedt, K. L.; Okabe, Y.; Head-Gordon, T., Protofibril Assemblies of the Arctic, Dutch, and Flemish Mutants of the Alzheimer's A β 1-40 Peptide. *Biophys. J.* **2008**, *94* (6), 2007-2016; (c) Pellarin, R.; Caflich, A., Interpreting the

- aggregation kinetics of amyloid peptides. *J. Mol. Biol.* **2006**, *360* (4), 882-892; (d) Abeln, S.; Vendruscolo, M.; Dobson, C. M.; Frenkel, D., A simple lattice model that captures protein folding, aggregation and amyloid formation. *PLoS one* **2014**, *9* (1), e85185.
19. Han, W.; Schulten, K., Fibril Elongation by A β 17–42: Kinetic Network Analysis of Hybrid-Resolution Molecular Dynamics Simulations. *J. Am. Chem. Soc.* **2014**, *136* (35), 12450-12460.
20. (a) Sorensen, J. M.; Head-Gordon, T., Toward minimalist models of larger proteins: A ubiquitin-like protein. *Proteins: Struct., Func., Bioinform.* **2002**, *V46* (N4), 368-379; (b) Sorensen, J.; Head-Gordon, T., Protein engineering study of protein L by simulation. *J. Comp. Bio.* **2002**, *9* (1), 35-54; (c) Brown, S.; Fawzi, N. J.; Head-Gordon, T., Coarse-grained sequences for protein folding and design. *Proc. Natl. Acad. Sci.* **2003**, *100* (19), 10712-10717; (d) Yap, E. H.; Fawzi, N. L.; Head-Gordon, T., A coarse-grained α -carbon protein model with anisotropic hydrogen-bonding. *Proteins: Struct. Funct. and Bioinf.* **2008**, *70* (3), 626-638.
21. (a) Brown, S.; Head-Gordon, T., Intermediates and the folding of proteins L and G. *Prot. Sci.* **2004**, *13* (4), 958-970; (b) Fawzi, N. L.; Chubukov, V.; Clark, L. A.; Brown, S.; Head-Gordon, T., Influence of denatured and intermediate states of folding on protein aggregation (vol 14, pg 993, 2005). *Prot. Sci.* **2005**, *14* (5), 1380-1380; (c) Marianayagam, N.; Fawzi, N.; Head-Gordon, T., Protein folding by distributed computing and the denatured state ensemble. *Proc. Natl. Acad. Sci.* **2005**, *102*, 16684-16689; (d) Sorensen, J.; Head-Gordon, T., Matching simulation and experiment: A new simplified model for protein folding. *J. Comp. Bio.* **2000**, *7* (3/4), 469-481; (e) Sorensen, J. M.; Head-Gordon, T., Redesigning the hydrophobic core of a model beta-sheet protein: Destabilizing traps through a threading approach. *Proteins: Struct., Func., Bioinform.* **1999**, *V37* (N4), 582-591.
22. Lu, J.-X.; Qiang, W.; Yau, W.-M.; Schwieters, C. D.; Meredith, S. C.; Tycko, R., Molecular structure of β -amyloid fibrils in Alzheimer's disease brain tissue. *Cell* **2013**, *154* (6), 1257-1268.
23. Tycko, R., Amyloid Polymorphism: Structural Basis and Neurobiological Relevance. *Neuron* **2015**, *86* (3), 632-645.
24. (a) Petkova, A. T.; Yau, W.-M.; Tycko, R., Experimental constraints on quaternary structure in Alzheimer's β -amyloid fibrils. *Biochemistry* **2006**, *45* (2), 498-512; (b) Paravastu, A. K.; Leapman, R. D.; Yau, W.-M.; Tycko, R., Molecular structural basis for polymorphism in Alzheimer's β -amyloid fibrils. *Proc. Natl. Acad. Sci.* **2008**, *105* (47), 18349-18354; (c) Xiao, Y.; Ma, B.; McElheny, D.; Parthasarathy, S.; Long, F.; Hoshi, M.; Nussinov, R.; Ishii, Y., A [beta](1-42) fibril structure illuminates self-recognition and replication of amyloid in Alzheimer's disease. *Nature Struct. Biol.* **2015**, *22* (6), 499-505.
25. Fawzi, N. L.; Yap, E. H.; Okabe, Y.; Kohlstedt, K. L.; Brown, S. P.; Head-Gordon, T., Contrasting disease and nondisease protein aggregation by molecular simulation. *Acc. Chem. Res.* **2008**, *41* (8), 1037-47.
26. Ball, K. A.; Phillips, A. H.; Wemmer, D. E.; Head-Gordon, T., Differences in β -strand populations of monomeric amyloid- β 40 and amyloid- β 42. *Biophys. J.* **2013**, *104* (12), 2714-2724.
27. Krzeminski, M.; Marsh, J. A.; Neale, C.; Choy, W.-Y.; Forman-Kay, J. D., Characterization of disordered proteins with ENSEMBLE. *Bioinformatics* **2013**, *29* (3), 398-399.
28. Ball, K. A.; Wemmer, D. E.; Head-Gordon, T., Comparison of Structure Determination Methods for Intrinsically Disordered Amyloid- β Peptides. *J. Phys. Chem. B* **2014**, *118*, 6405-6416.
29. Kabsch, W.; Sander, C., Dictionary of protein secondary structure: pattern recognition of hydrogen-bonded and geometrical features. *Biopolymers* **1983**, *22* (12), 2577-2637.

30. Andersen, H. C., RATTLE: A “Velocity” version of the SHAKE algorithm for molecular dynamics calculations. *J. Comput. Phys.* **1983**, *52* (1), 24-34.
31. Ferrone, F., [17] Analysis of protein aggregation kinetics. *Methods Enzymol.* **1999**, *309*, 256-274.
32. Lindorff-Larsen, K.; Piana, S.; Palmo, K.; Maragakis, P.; Klepeis, J. L.; Dror, R. O.; Shaw, D. E., Improved side-chain torsion potentials for the Amber ff99SB protein force field. *Proteins: Struct. Funct. and Bioinf.* **2010**, *78* (8), 1950-1958.
33. Horn, H. W.; Swope, W. C.; Pitara, J. W.; Madura, J. D.; Dick, T. J.; Hura, G. L.; Head-Gordon, T., Development of an improved four-site water model for biomolecular simulations: TIP4P-Ew. *J. Chem. Phys.* **2004**, *120* (20), 9665-9678.
34. Van Der Spoel, D.; Lindahl, E.; Hess, B.; Groenhof, G.; Mark, A. E.; Berendsen, H. J., GROMACS: fast, flexible, and free. *J. Comp. Chem.* **2005**, *26* (16), 1701-1718.
35. Darden, T.; York, D.; Pedersen, L., Particle mesh Ewald: An $N \cdot \log(N)$ method for Ewald sums in large systems. *J. Chem. Phys.* **1993**, *98* (12), 10089-10092.
36. Humphrey, W.; Dalke, A.; Schulten, K., VMD: visual molecular dynamics. *J. Mol. Graph.* **1996**, *14* (1), 33-38.
37. O’Nuallain, B.; Shivaprasad, S.; Kheterpal, I.; Wetzel, R., Thermodynamics of A β (1-40) amyloid fibril elongation. *Biochemistry* **2005**, *44* (38), 12709-12718.

TABLES

Table 1: Sequence mapping from all-atom AD fibril structure to CG fibril model.

Amino acid sequence	DAEFRHDSGY EVHHQKLVFF AEDVGSNKGA IIGLMVGGVV
CG bead sequence	LVLBLNBBBB LVNNLNBVBB VLLVBBBNNB BBNBBVNNBB
Secondary Structure	TTTTTTTTE EEEETEEEEEE EETTTTTEE EEEEEEE
Hydrogen bonding	CCCCCCCBB BBBB BBBB BBBCCCCBB BBBB BBBB

Table 2: Monomer potentials for different monomer ensembles used in fibril addition studies

Fibril ensemble	Bead flavor	same as protofibril model
	Secondary Structure	same as protofibril model
	Hydrogen bonding	same as protofibril model
Random ensemble	Bead flavor	same as protofibril model
	Secondary Structure	TTTTTTTTTT TTTTTTTTTT TTTTTTTTTT TTTTTTTT
	Hydrogen bonding	XXXXXXXXXX XXXXXXXXXXXX XXXXXXXXXXXX XXXXXXXXXX
IDP ensemble	Bead flavor	same as protofibril model
	Secondary Structure	based on the secondary structure propensity of each structure
	Hydrogen bonding	based on the secondary structure propensity of each structure
Activated ensemble	Bead flavor	LVLBLNBBBB LVNNLNBVBB VLLVBBBNNB BBNBBVNNBB
	Secondary Structure	TTTTTTTYYY YYYYYYYYYY YPTYYTQYYY YYYYYYY
	Hydrogen bonding	CCCCCCCXXX XXXXXXXXXXXX XCCCCCXXX XXXXXXXXXX

Table 3: Free energy of binding for fibril elongation at the two fibril tips by monomer addition.

	Monomer Ensemble (in units of $k_B T$)			
	<i>Fibril</i>	<i>Random</i>	<i>IDP</i>	<i>Activated</i>
C-terminus	13.7 ± 0.74	14.3 ± 0.33	14.2 ± 0.18	13.6 ± 0.22
N-terminus	13.3 ± 0.30	14.2 ± 0.31	13.6 ± 0.23	13.5 ± 0.13

Table 4: Ratio of locking to docking time scales for monomer addition at the two fibril ends.

	Monomer Ensemble $\tau_{\text{lock}}/\tau_{\text{dock}}$			
	<i>Fibril</i>	<i>Random</i>	<i>IDP</i>	<i>Activated</i>
C-terminus	11.8 ± 5.0	9.4 ± 4.0	6.5 ± 2.4	4.1 ± 1.0
N-terminus	29.3 ± 28.2	8.9 ± 3.2	13.7 ± 7.7	15.2 ± 15.1

FIGURE CAPTIONS

Figure 1: Structure of the A β 40 polymorph isolated from the brain tissues of an Alzheimer's patient, with 3-fold symmetry based on solid state NMR studies by Lu et al ²². The aqua region is the central hydrophobic core consisting of residues 12-24 and the blue region highlights the C-terminal hydrophobic residues 30-40.

Figure 2. Fibril stability parameters $\langle \chi_f \rangle$ and $\langle P_f \rangle$ for equilibrated protofibrils consisting of 6-30 peptide chains. The parameters give a measure of how much the protofibril structure has deviated from the ideal fibril, with a value of 1 representing perfect fibril structure. Statistics are based on 3 different sets of simulations for each initial protofibril structure.

Figure 3. Snapshot of an unstable protofibril containing 15 peptide chains, where one of the monomers in the outermost cross-section has formed an intra-molecular β -strand (red strand) with the C-terminal residues (blue region), by breaking a part of the N-terminal inter-molecular β -sheet formed by residues 10-22.

Figure 4. Free energy profile for the protofibril and free monomer equilibrium. The critical nucleus size is about 12 peptide chains with the constant negative slope beyond the critical nucleus size indicating favorable region of fibril growth via monomer addition.

Figure 5. Fibril stability parameters $\langle \chi_f \rangle$ and $\langle P_f \rangle$ for equilibrated protofibrils using an all-atom simulation. Statistics are based on the last 30 ns of 100 ns simulations for 2-5 cross-sections.

Figure 6: The potential of mean force profile for monomer addition at the two fibril tips as a function of separation distance r_c (a) from monomer configurations drawn from the Fibril ensemble, and (b) Activated ensemble. The free energy profile is very similar for the all four monomer ensembles, with a single minima.

Figure 7. MFPT required to form the first non-native (docking) and the first native contacts (locking) for different monomer ensembles. All the four monomer ensembles have two different time-scales for forming the first non-native and native contacts, indicating that the "lock-dock" mechanism is the more common mechanism for fibril elongation, irrespective of the monomer structure. Nonetheless the activated form has the smallest separation of dock and lock timescales. (a) formation of 5 non-native and 5 native contacts. (b) formation of 10 non-native and 10 native contacts, which shows that our conclusions are not dependent on number of contacts.

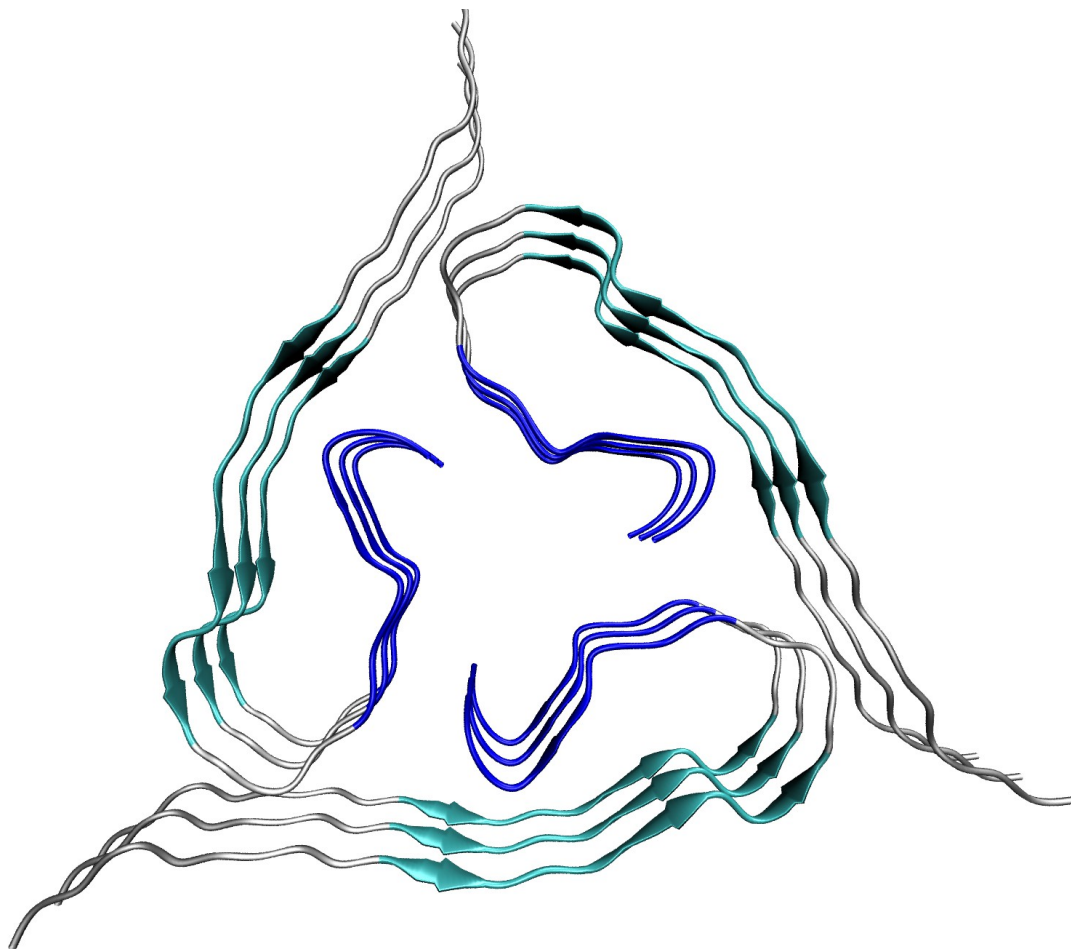


Figure 1. Sasmal, Schwierz, Head-Gordon

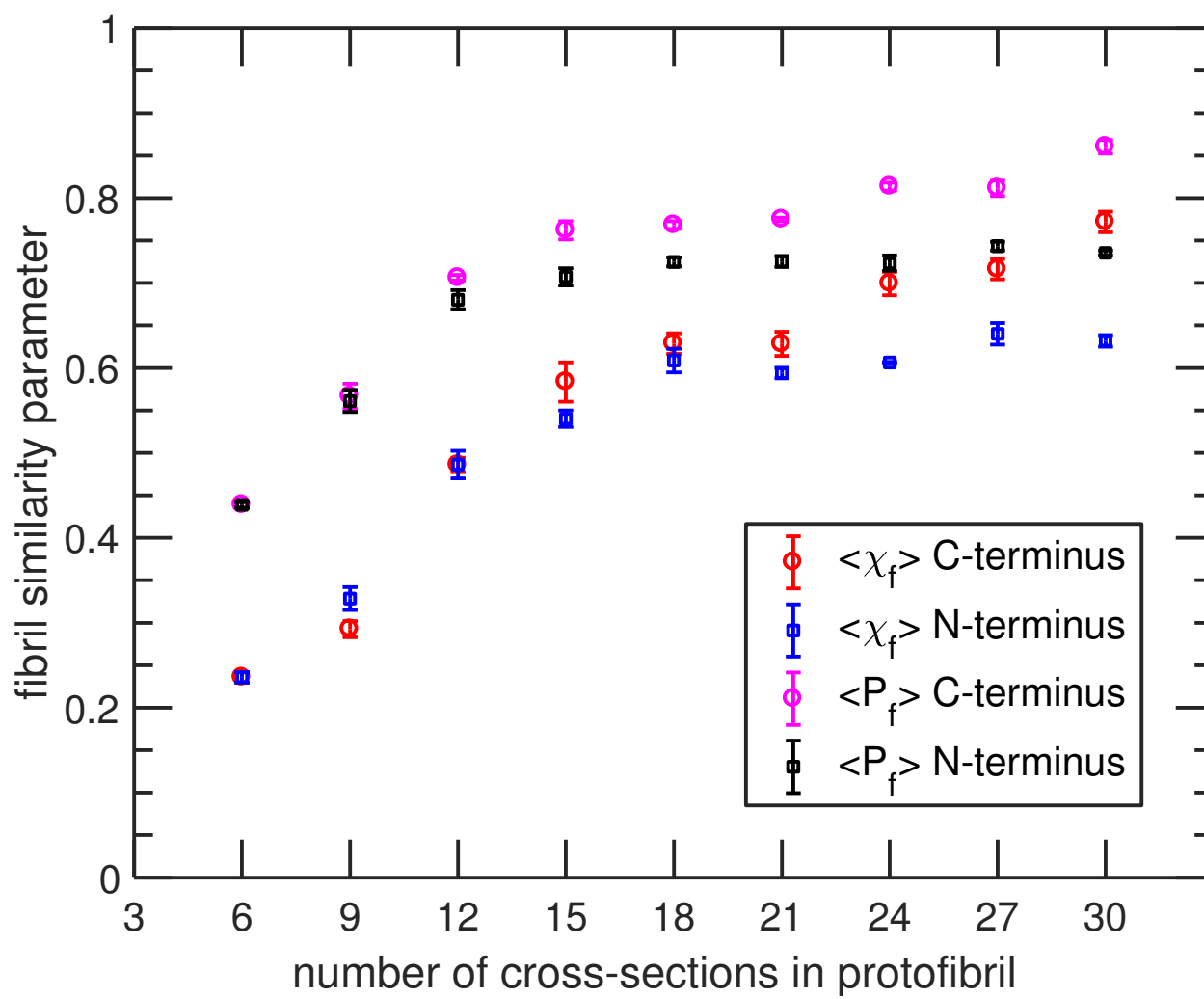


Figure 2. Sasmal, Schwierz, Head-Gordon

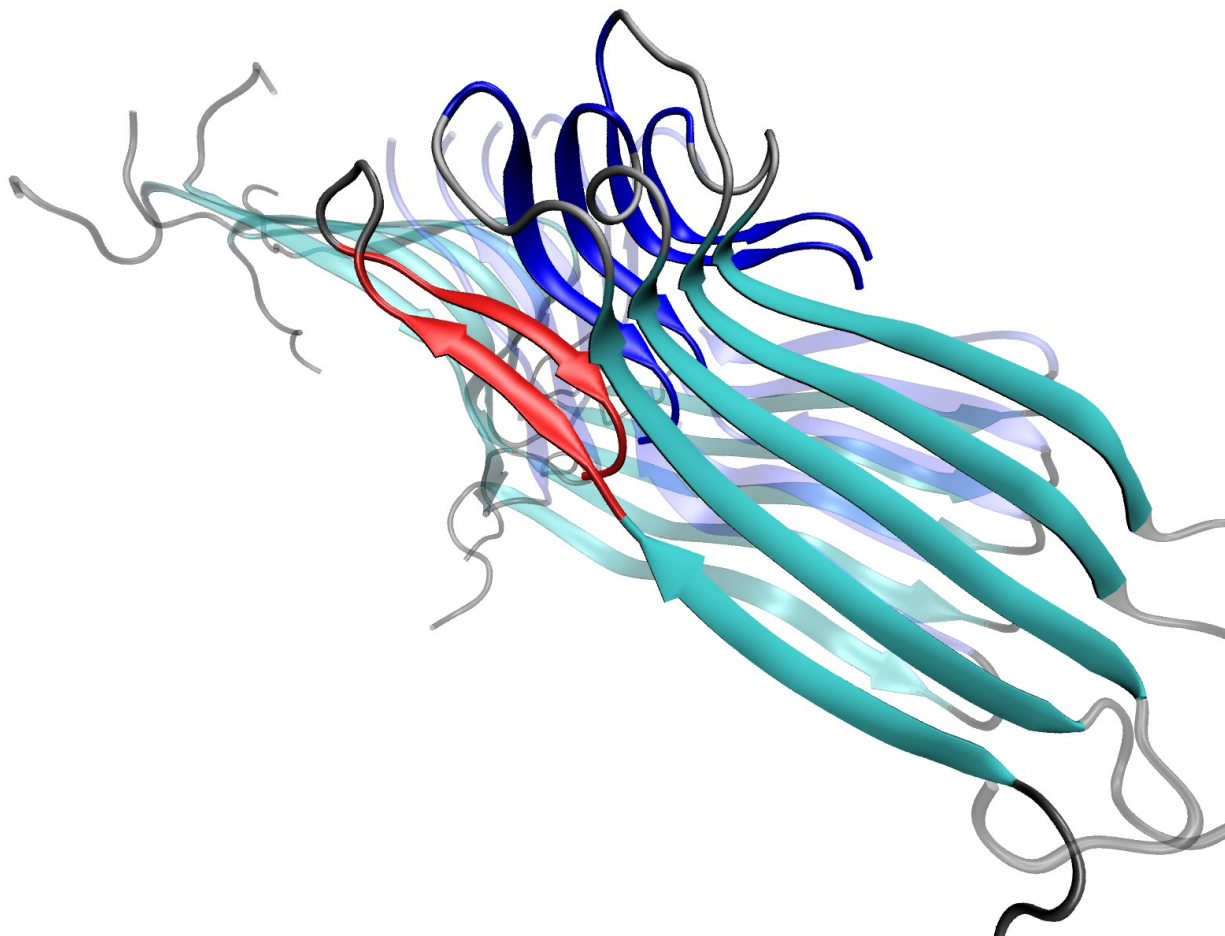


Figure 3. Sasmal, Schwierz, Head-Gordon

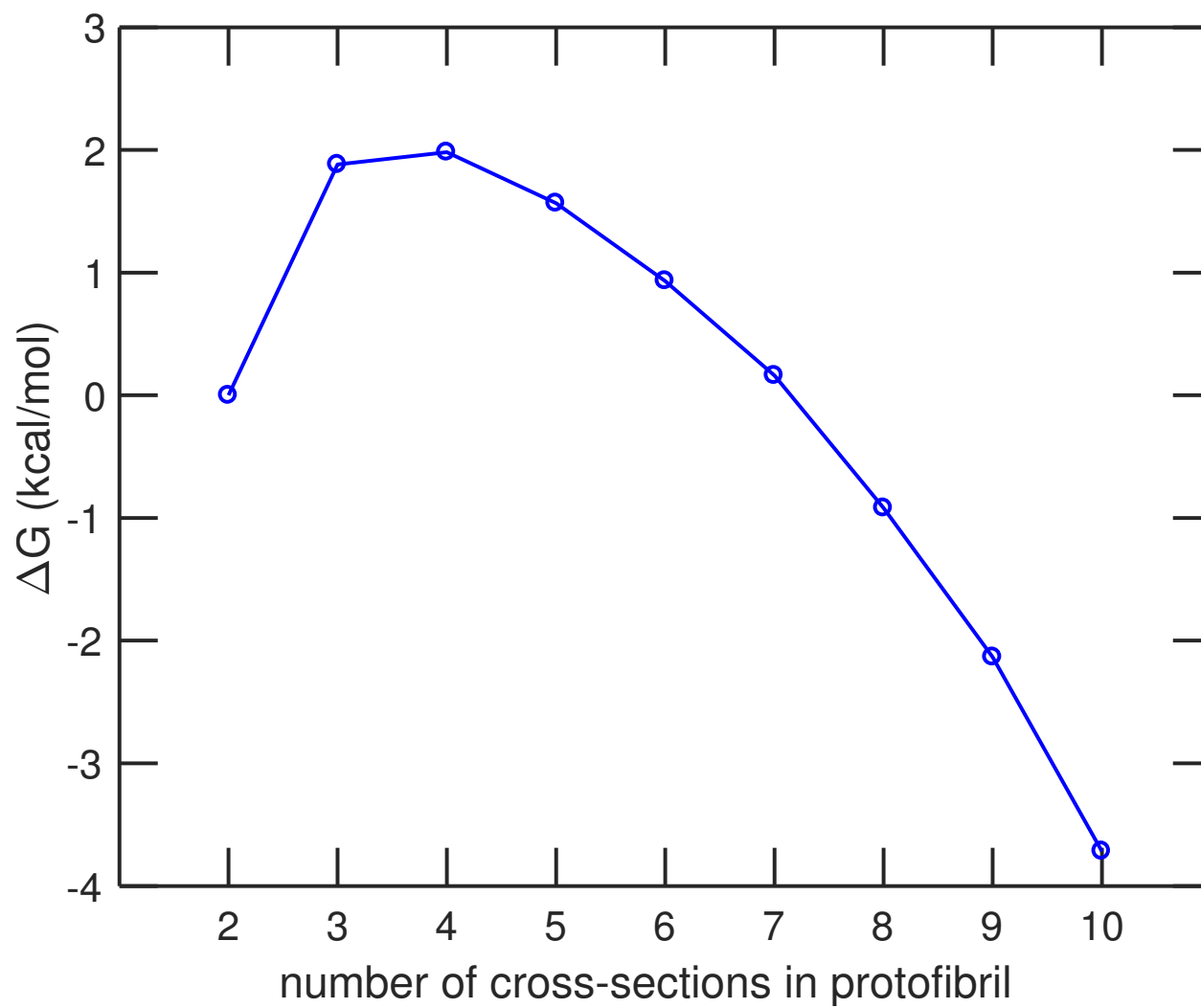


Figure 4. Sasmal, Schwierz, Head-Gordon

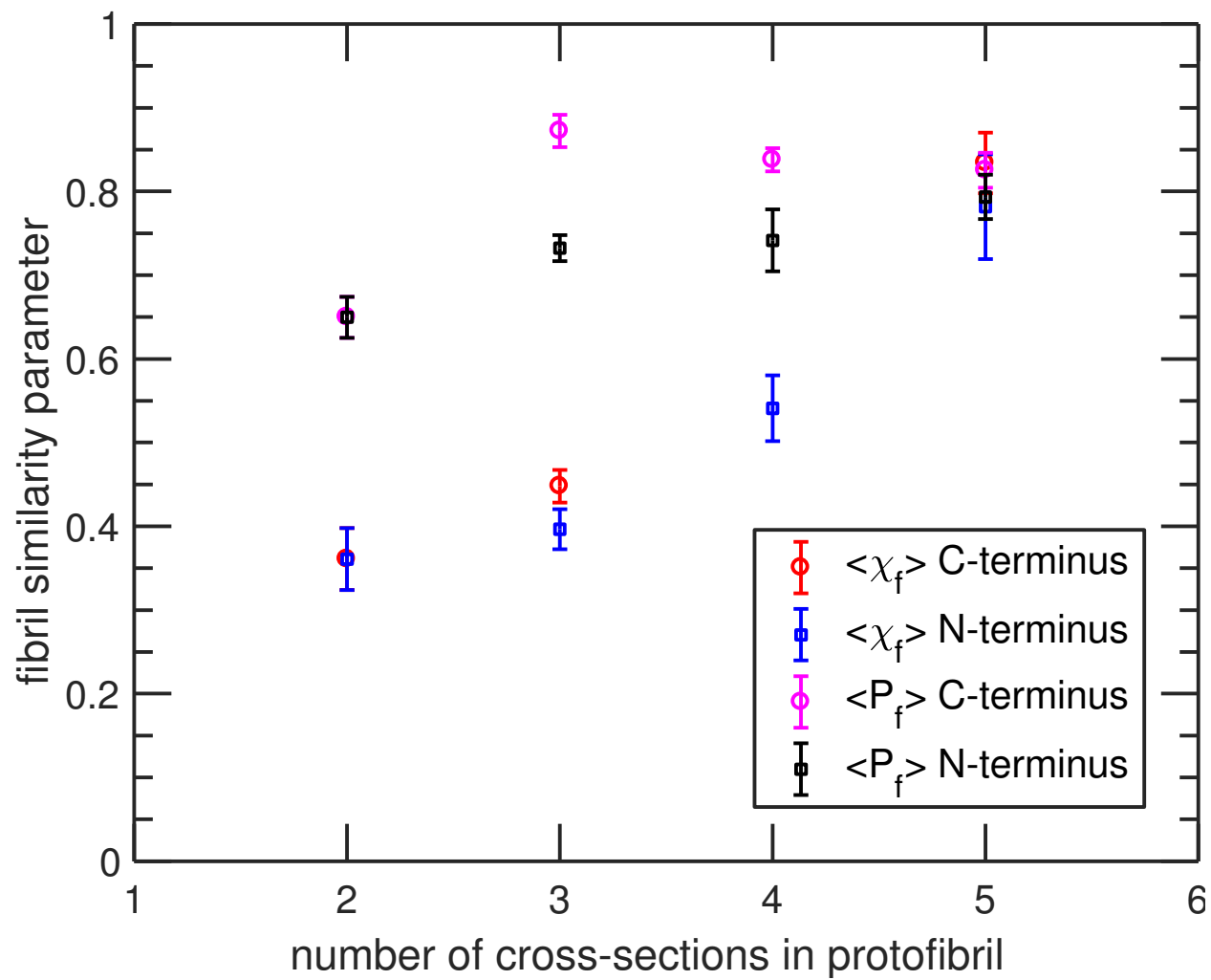


Figure 5. Sasmal, Schwierz, Head-Gordon

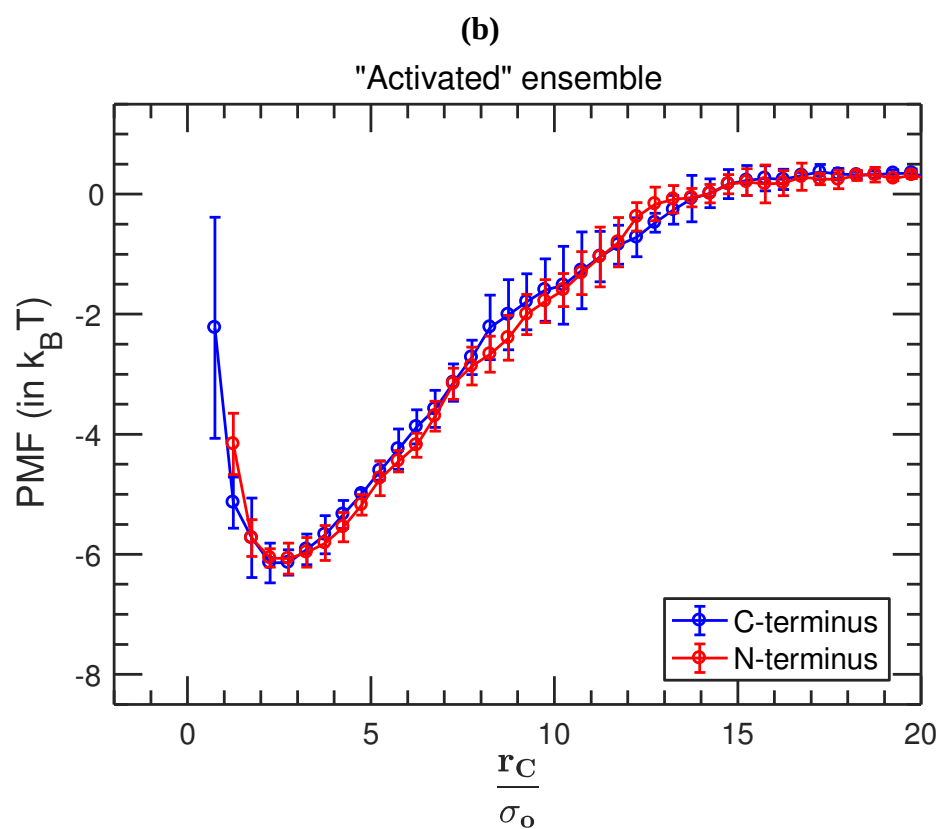
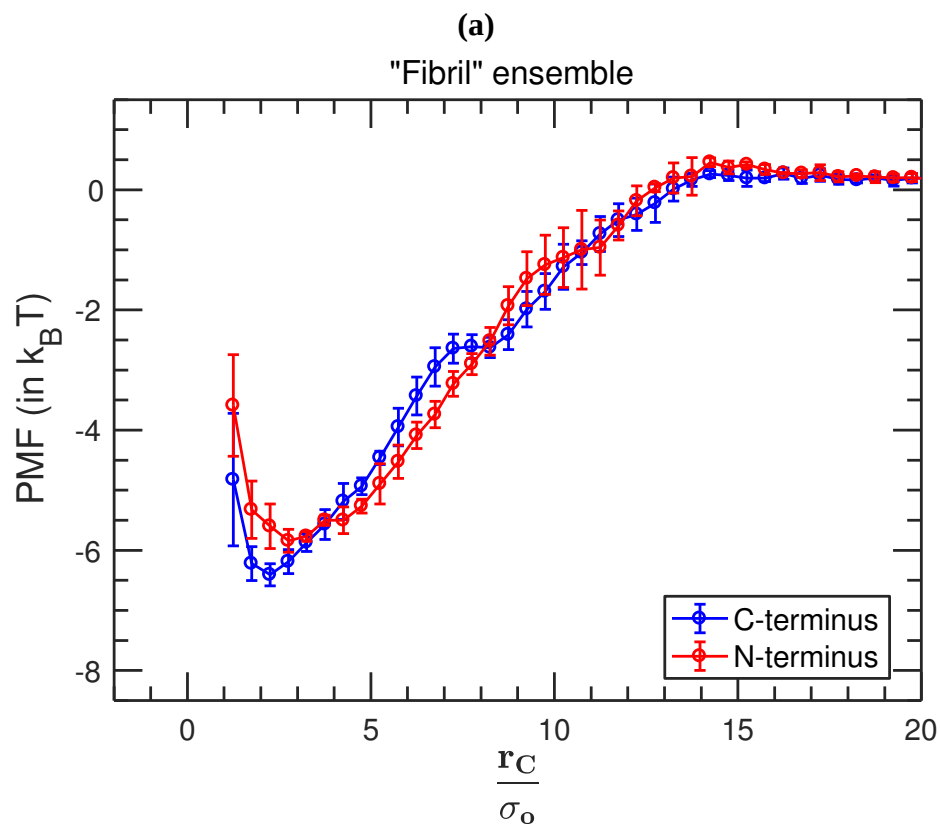


Figure 6. Sasmal, Schwierz, Head-Gordon

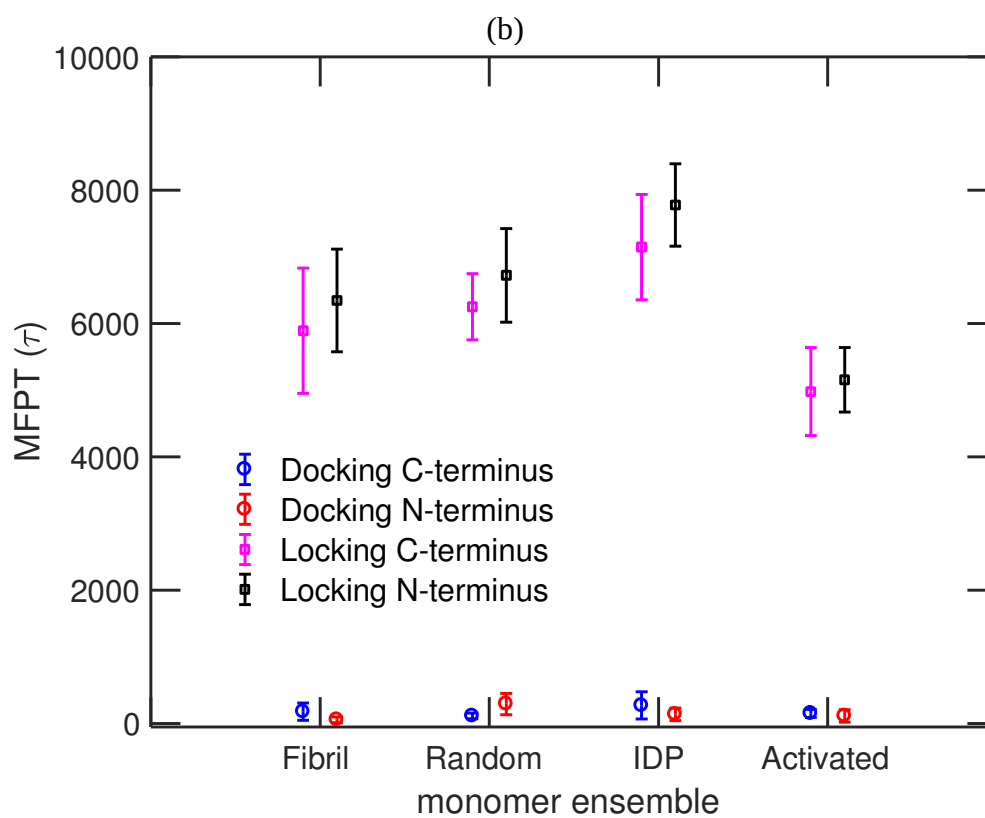
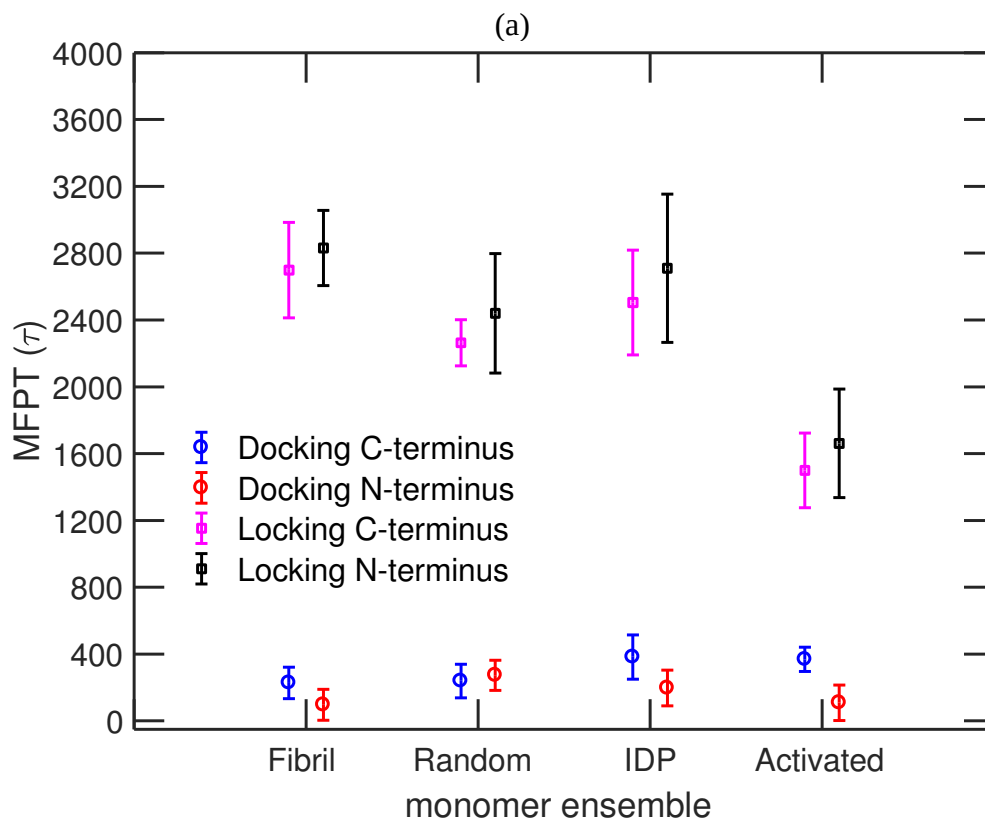


Figure 7. Sasmal, Schwierz, Head-Gordon

TOC GRAPHIC

